New signal processing techniques for phased-array oceanographic radars: self-calibration, antenna grouping, and denoising

Dylan Dumas, Charles-Antoine Guérin

New signal processing techniques for phased-array oceanographic radars: self-calibration, antenna grouping, and denoising

Dylan Dumas and Charles-Antoine Guérin

MIO, Université de Toulon, Aix-Marseille Univ, CNRS, IRD, Toulon, France

Corresponding author: Charles-Antoine Guérin, guerin@univ-tln.fr

ABSTRACT: Original techniques are proposed for the improvement of surface current mapping with phased-array oceanographic High-Frequency Radars. The first idea, which works only in bistatic configuration, is to take advantage of a remote transmitter to perform an automatic correction of the receiving antennas based on the signal received in the direct path, an adjustment that is designated as "self-calibration". The second idea, which applies to both mono- and bistatic systems, consists in applying a Direction Finding (DF) technique (instead of traditional Beam Forming) not only to the full antenna array but also to subarrays made of a smaller number of sequential antennas, a method which is referred to as "antenna grouping". In doing this, the number of sources can also be varied, leading to an increased number of DF maps that can be averaged, an operation which is designated as "source stacking". The combination of self-calibration, antenna grouping, and source stacking makes it possible to obtain high-resolution maps with increased coverage and is found robust to damaged antennas. The third improvement concerns the mitigation of noise in the antenna signal. These methods are illustrated with the multistatic High-Frequency Radar network in Toulon and their performances are assessed with drifters. The improved DF technique is found to significantly increase the accuracy of radar-based surface current when compared to the conventional Beam Forming technique.

1. Introduction

High-Frequency Radars (HFR) are routinely used for the mapping of coastal surface currents. The main physical principle underlying this detection has been unveiled in the pioneering works of Crombie (Crombie 1955) and Barrick (Barrick 1972). It relies on measuring the Doppler shift induced by the radial surface current on the backscattered sea echo. This is made possible by the presence of a couple of very marked peaks in the Doppler spectrum, referred to as the "Bragg lines". This terminology alludes to a grating effect that is observed in HFR scattering from gravity waves and which is similar to the resonant mechanism observed in X-ray Bragg diffraction from crystals. There is abundant literature on the estimation of surface currents from HFR and the associated applications (see e.g. the review papers Paduan and Graber (1997); Headrick and Thomason (1998); Paduan and Washburn (2013); Wyatt (2014); Roarty et al. (2019); Reyes et al. (2022); Lorente et al. (2022)) and there is no need to go into details. It is sufficient to say that the extraction of surface current maps from HFR antenna voltage results from a complex but universal chain of signal processing steps. Most HFR systems are monostatic, that is have co-located transmitters and receivers, and use pairs of radar to infer two radial components from which the surface current vector can be recombined. In some cases, it is advantageous to operate in a bistatic configuration (e.g. Grosdidier et al. (2014)) in which the transmitter and receiver are located remotely or even multistatic systems, which are a combination of remote transmitters and receivers (e.g. Dumas et al. (2020)).

The aforementioned chain of processing is common to monostatic and bistatic configuration with some adaptation in the geometrical formulas (see e.g. Lipa et al. (2009)). For a bistatic pair of (TX, RX) the iso-range radar cells follow ellipses with focal points at the transmitter and receiver locations (as opposed to circles around the transmitter in the monostatic case). The resonant Bragg frequency f_B in the Doppler spectrum depends on the bistatic angle φ (with $f_B^2 = g\cos\varphi/(\pi\lambda)$) hence on the sea surface patch, while it is constant in the monostatic case (with $f_B^2 = g/(\pi\lambda)$). Any observed Doppler shift Δf with respect to this local Bragg frequency is proportional to the projected component U_n of the surface current vector $\boldsymbol{U}$ onto the normal direction to the ellipse, which is referred to as the elliptical velocity ($U_n = \lambda\Delta f/(2\cos\varphi)$. In the monostatic case, this frequency shift is proportional to the radial component U_r of the surface current vector along the radar look direction, ($U_r = \lambda\Delta f/2$).

The most critical and system-dependent operation in processing HFR data for producing current maps is the azimuthal discrimination of the backscattered antenna signal. For linear or quasi-linear extended arrays of antennas, this is usually done with a Beam Forming (BF) technique which allows steering the bearing angle by numerically adjusting the relative phase shifts of the antenna signals (e.g. Gurgel et al. (1999b)). This makes it possible to continuously sweep the angular sector covered by the radar. However, the resulting azimuthal accuracy depends on the array extension and deteriorates as the steering angle deviates from the central direction. Compact antenna systems rely on high-resolution methods such as Direction Finding (DF) techniques with the weak point being that this requires longer integration time, produces lacunary maps, and is more prone to errors. These two techniques will be analyzed and compared in the following sections in context of the HFR network in Toulon. This last system has been operated for one decade in bistatic mode and is running in multistatic mode as of January 2019 (Grosdidier et al. (2014); Guérin et al. (2019); Dumas et al. (2020)). While developing specific software for the azimuthal processing of these data in such a nonstandard configuration we made use of a novel opportunity offered by the bistatic mode, namely a possible instantaneous calibration of the receiving antenna with the direct signal of the remote transmitter. The idea of using opportunistic external sources for calibration is not new (see e.g. Solomon et al. (1999); Fernandez et al. (2003); Kohut and Glenn (2003); Washburn et al. (2017); Emery et al. (2014)) but this technique avoids running dedicated campaigns that require the deployment of ships, aerial drones, or other external sources.

This simple and automatic technique is referred to as a "self-calibration" method since it does not require any specific action from the operator (besides an additional line of code in the software) and can be performed in real-time for every time series. As seen later, an hourly update of the array calibration is necessary as the required phase corrections follow a diurnal cycle and a seasonal evolution. Another original aspect of the historical network was the limited extension and irregular form of the initial antenna arrays (8 antennas from 2012 to 2018) which led its first operators to develop high-resolution DF methods (Barbin et al. (2009); Barbin (2011)). The antenna arrays were extended to 12-antenna linear arrays in 2019 and 2020 but the idea of using DF for non-compact arrays was maintained and improved. In 2019 an improved DF technique was devised, based on testing multiple subarrays, a method that was termed "antenna grouping". The self-calibration and antenna grouping techniques are currently running on-site for the processing of near real-time HFR

data in Toulon (http://hfradar.univ-tln.fr/) and have been used for the reprocessing of historical data (2012-2018). This HFR network will be briefly presented in Section 2 and the following sections will introduce the self-calibration method (Section 3), the antenna grouping method (Section 4), and the noise mitigation techniques (Section 5). When used together, these methods allow for a significant improvement of surface current mapping in terms of accuracy, coverage, and robustness to hardware failure. An assessment of the accuracy of these novel techniques and comparison with classical BF is performed in the light of a drifter campaign (Section 6).

2. The HFR in Toulon

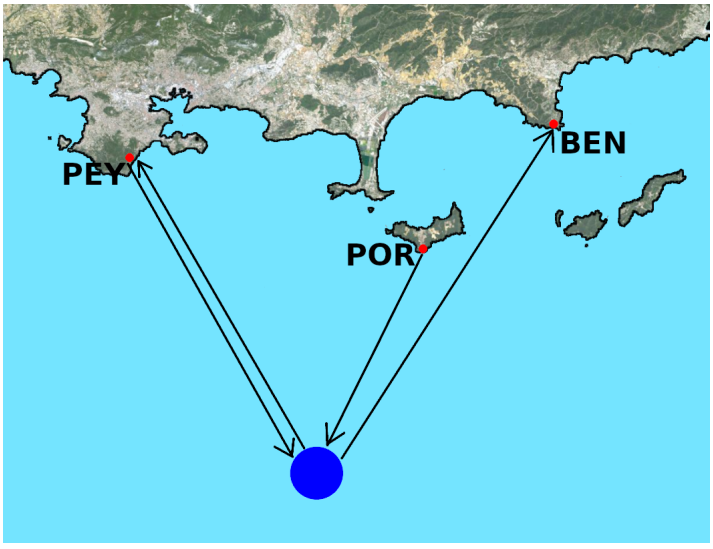

FIG. 1. The three HFR sites in the region of Toulon: 1) Fort Peyras (TX/RX, "PEY"); 2) Cap Bénat (RX, "BEN"); 3) Porquerolles Island (TX, "POR").

The HFR network in Toulon is manufactured by WERA Helzel Messtecknik. It is composed of 2 transmitters and 2 receivers located on three distant sites (Figure 1). A standalone transmitter is located on Porquerolles Island, 27 km South-East of Toulon; its single, non-directional, emitting antenna illuminates a wide sea area to the South. The first receiver is located at Cap Bénat, 35 km East of Toulon, with a regular linear array of 12 receiving active antennas (70 deg from North, anticlockwise) with 0.45 λ spacing. The second transmitter and receiver are located at Fort Peyras about 8 km South West of Toulon. The receiving array is composed of a linear array of 12 passive antennas along the North-South direction with a 0.45λ spacing as well. Note that the present

combination of 2 TX and 2 RX leads to 3 bistatic pairs and 1 monostatic pair which can be used for the surface current vector reconstruction. One can refer to (Gurgel et al. 1999a) for a detailed account of the processing of the radar signal and to (Guérin et al. 2019) for its adaptation to the multistatic mode. Range gating is obtained by the standard frequency-modulated continuous wave (FMCW) HFR technology. The two transmitters POR and PEY send continuous chirp ramps of duration 0.26 seconds within a frequency band of 100 kHz around the same central frequency $f = 16.150$ MHz, allowing for a 1.5 km range resolution. In FMCW HF radar technology, the range gating is obtained by Fourier Transforming the radar signal on the fast time and binning the received signal in frequency shifts (Gurgel and Schlick 2009). A complex Doppler spectrum is calculated for every single range cell and antenna by Fourier Transform of the recorded voltage time series at the slow time, that is at the chirp rate. Its squared modulus is referred to as the omnidirectional Power Spectral Density (PSD). In order for the receivers to discriminate the signal scattered from the two different sources, the two emitting central frequencies are offset by a multiple of a frequency bin in such as way that the first half of the range cells is allocated to one transmitter and the other half to the second transmitter. Figure 2 shows typical range-Doppler maps obtained by processing the range-resolved temporal signal received on a single antenna in Cap Bénat and Fort Peyras, respectively. The first "floor" corresponds to the bistatic sea echo from the Fort Peyras transmitter while the second floor is the bistatic return from the Porquerolles transmitter. Note the typical features of the bistatic Range-Doppler spectrum, that is U-shaped Bragg lines and an offset in the range corresponding to half the straight distance between transmitter and receiver.

3. Self-calibration of antenna arrays

a. Beam-Forming and its issues

For extended antenna arrays, BF is the traditional method to discriminate the radar signal in azimuth. Consider the canonical problem of a periodic linear array of N identical antennas with spacing d, illuminated by a plane wave with wavenumber $K = 2\pi/\lambda$ incoming from a direction θ_s measured from the normal to the array. In the absence of noise and assuming a perfectly coherent monochromatic incident wave, the complex time series recorded on the I&Q channels of each antenna is proportional to $e^{i2\pi ft}S_n$, where f is the radar frequency and S_n is a complex antenna gain depending only on the source direction θ_s. For simplicity, the antennas are assumed to have

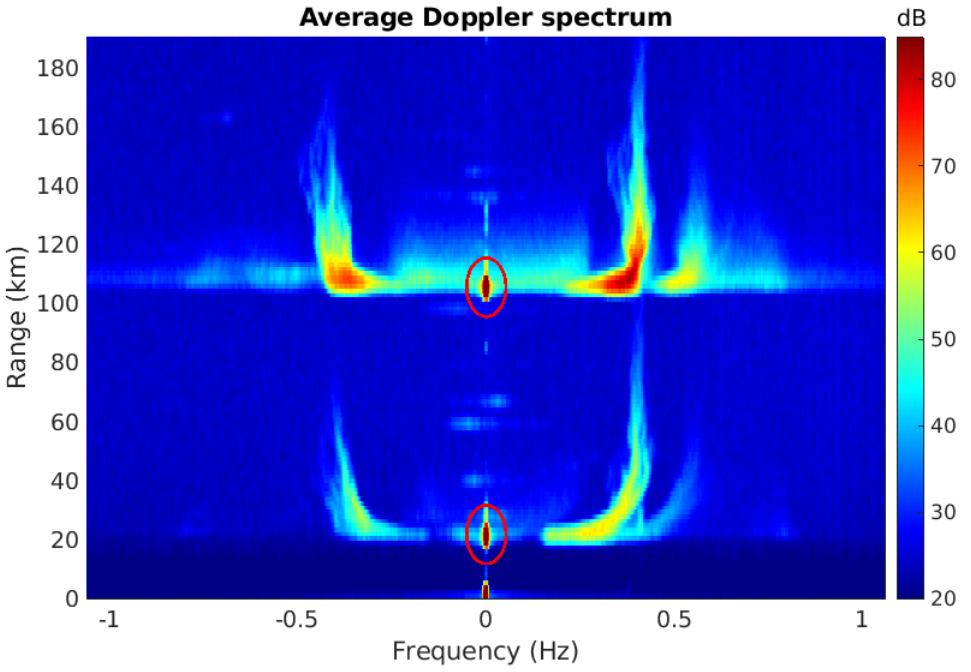

FIG. 2. Bistatic Range-Doppler spectra on the Bénat receiver with 2 simultaneous transmitters. The upper floor corresponds to the Porquerolles transmitter and the lower floor to the Peyras transmitter. The direct signal from the transmitter to the receiver is a strong echo at the zero-Doppler cell (red circles)

the same unit gain in amplitude and to differ only by a phase shift. Once normalized by the first antenna, the complex signal S_n on the nth antenna depends only on its position in the array and the direction of the source:

$$S_n = e^{-i(n-1)Kd\sin\theta_s} \tag{1}$$

The so-called Array Factor (Balanis (2016)):

$$AF(\theta) = \sum_{n=1}^{N} e^{i(n-1)Kd(\sin\theta - \sin\theta_s)} \tag{2}$$

gives the remote electric far-field amplitude that would be produced by an array of identical radiators S_n by the principle of reciprocity. It is maximal in the direction of the source $\theta = \theta_s$ with a main lobe of width $\lambda/(Nd)$. An array factor can also be defined for irregular arrangements. This is important as the site topography often prevents the installation of the complete array along a straight line. Denoting $\boldsymbol{d_n}$ the relative vector position of the nth antenna with respect to the first

one, the array factor for an incoming source in direction θ_s can be written as:

$$AF(\theta) = \sum_{n=1}^{N} e^{+iK(\boldsymbol{u}(\theta)-\boldsymbol{u}(\theta_s))\cdot \boldsymbol{d_n}} \tag{3}$$

where $\boldsymbol{u}(\theta)$ is the outgoing unit vector in direction θ. For later use note that the array factor can be expressed as a scalar product between the so-called steering vectors in direction of the source (θ_s) and in direction of observation (θ):

$$AF(\theta) = \boldsymbol{a}(\theta) \cdot \boldsymbol{a}(\theta_s)^*, \tag{4}$$

where the steering vector is defined as:

$$\boldsymbol{a}(\theta) = \left(1, e^{iK\boldsymbol{u}(\theta)\cdot \boldsymbol{d_1}}, ..., e^{iK\boldsymbol{u}(\theta)\cdot \boldsymbol{d_N}}\right) \tag{5}$$

BF consists in re-radiating the received complex multidimensional signal $\boldsymbol{S} = (S_1, ..., S_N)$ at infinity while continuously steering the angle θ in the array factor to unveil all incoming sources. This is done for each chirp number and range index so that in the end the following complex time series is obtained as a function of range (R), bearing (θ) and time (t):

$$X(R, \theta, t) = \boldsymbol{a}(\theta) \cdot \boldsymbol{S}^*(R, t) \tag{6}$$

A directional PSD can be obtained with the square modulus of the Fourier Transform of this matrix along the time axis leading to the so-called directional Range-Doppler spectra. The angular spread of the AF determines the accuracy and the quality of the azimuthal discrimination and therefore the resolution of the Bragg lines in the directional Doppler spectra. In particular, secondary lobes can be an important source of error if insufficiently rejected since they may "capture" strong sources (through their Bragg lines) away from the focusing direction. Secondary lobes can be efficiently rejected by using a tapering window but the azimuthal resolution remains bound to the array extent. In addition, the perturbations of the electromagnetic environment as well as the misalignment of the antennas induce phase shifts with respect to the theoretical values which depend only on the array geometry. This results in a deformation of the array factor with possible mispointing and

enhancement of secondary lobes. The phase perturbation can induce a mispointing of a few degrees and a strong enhancement of secondary lobes. This will cause a systematic error in the direction of arrival of any source.

b. Self-calibration with one single source

The classical technique for HFR antenna calibration is based on using a transponder on a boat trip surrounding the emission site and measuring the complex response of each antenna, the so-called antenna manifold. This operation is in general time and money-consuming, requires dedicated manpower, and can only be performed once in a while. However, one can take advantage of the bistatic configuration to calibrate the antennas using the direct signal of the remote transmitter. The direct signal refers to the EM wave train which propagates in a straight line from the transmitter to the receiver without being scattered by sea surface patches on the travel path. It corresponds to the minimal bistatic distance, which is the distance between the transmitting and receiving sites. It is also concentrated on the zero-Doppler cell because this source is not Doppler-shifted by waves. The direct signal is therefore a strong echo concentrated on a particular cell in the range-Doppler map. It can be seen in Figure 2 as the red spots inside the red circles. The complex direct signal D_n recorded on the nth antenna can thus be extracted from the zero-Doppler cell at the minimal range after range and Doppler processing of the I and Q signals. Now, from the receiving array point of view, the direct signal is that from an incoming plane wave in direction θ_s of the transmitter. It should therefore produce the expected relative phase shifts $-K\boldsymbol{u}(\theta_s)\cdot\boldsymbol{d}_n$ ($=-(n-1)Kd\sin\theta_s$ for a linear periodic array). In terms of complex gain, this means:

$$D_n = e^{-iK(\boldsymbol{u}(\theta_s)\cdot\boldsymbol{d}_n)}D_1 = e^{i\phi_n}D_1 \tag{7}$$

The idea of self-calibration is to compare the theoretical geometrical phase shift between antennas to the actual phase shift measured from the direct signal. The difference between the expected and actual phase shift is a phase perturbation that should be compensated for when processing the antenna signals in azimuth. This idea has been already proposed to calibrate antenna arrays from ships equipped with transponders (Fernandez et al. 2003) but is more challenging to make automatic in this context. Using the signal from a remote transmitter at a fixed and known location allows for a complete automatization of the procedure.

The self-calibration procedure, therefore, runs as follows:

1. For each chirp and each antenna, extract the complex direct signal $\tilde{D}_n$ on each antenna by retaining the zero-Doppler/minimal range cell from the range-resolved I & Q signal and calculate its phase $\tilde{\phi}_n = \arg(\tilde{D}_n/\tilde{D}_1)$ relative to the first antenna in the array.

2. Calculate the phase difference $\delta\phi_n = \tilde{\phi}_n - \phi_n$ with respect to a theoretical array illuminated by a plane wave in direction of the transmitter (θ_s).

3. Before extracting the directional signal $X(R,\theta,t)$ as in (6), correct the complex antenna gain by this phase difference:

$$\tilde{S}_n(R,t) = S_n(R,t)e^{i\delta\phi_n} \tag{8}$$

By doing this it is assumed that the phase corrections $\delta\phi_n$ do not depend on the bearing θ. This important property is not granted *a priori* and the only certitude is that these phase corrections are appropriate in the direction θ_s of the transmitter. We, therefore, need the additional assumption that the required phase corrections $\delta\phi_n$ do not vary (at least, not appreciably) with the bearing. This is the main weakness of the method as compared to classical boat calibration, where all bearings can in principle be tested. Nevertheless, the calibration error resulting from a constant phase correction can be evaluated whenever a second remote transmitter is available since the direct signal in this last direction can also be extracted and compared with the predicted and corrected phase shifts using the first transmitter. This was done with the Bénat receiver using the Peyras and Porquerolles transmitters, which are separated by about 50 degrees in bearing. We found an RMS phase error of 20 degrees as compared to 32 degrees without any correction. As will be seen in the next subsection, this can be further improved by using multiple source calibration. Again, the main advantage of self-calibration over dedicated in situ campaigns is that it can be automatically updated at each radar observation cycle (in our case, one hour) and can therefore follow the natural evolution of the array response in time. The hourly variations of the Bénat receiver calibration phases were investigated over 3 weeks (November 4-24, 2020, corresponding to the drifters period in Section 6) with the Porquerolles emitter (Figure 3). As seen, the phase corrections can vary by about ±10 degrees from a mean over timescales of a few hours or longer. A diurnal cycle is visible in the variations as well as some abrupt changes (at hour 100 and 300). We hypothesize that this is caused by changes in humidity and temperature that would affect the cables and antenna

impedances as well as the antenna grounding to earth. It shows in any case that the instantaneous picture provided by a one-time ship or drone campaign is only approximate when used over a longer period. Even though the phase variations remains small, they appear to be stronly correlated from one antenna to another. Hence, neglecting these corrections could induce an overall mispointing of the array of the same order of magnitude (that is, ±10 degree) while steering the observation angle.

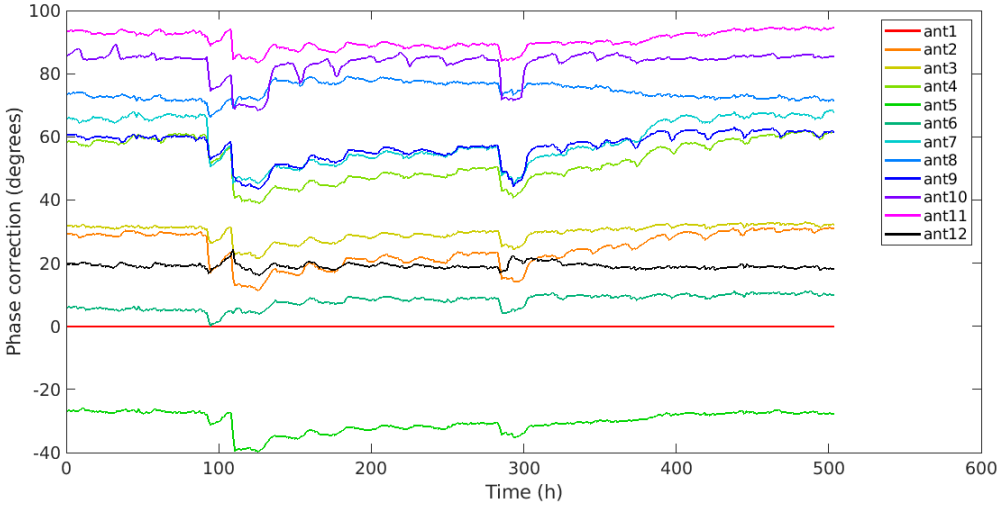

FIG. 3. Hourly variations of the self-calibration phases obtained with the Porquerolles emitter on the Bénat receive array. Antenna 1 is the reference.

.

Figure 4 shows two examples of elliptical/radial velocity maps obtained by processing one hour of data from each receiver. The azimuthal processing has been performed using the BF technique without (left panel) and with (right panel) self-calibration of the complex antenna gains. As seen, this makes important changes in the radial current map. The uncalibrated version shows disconnected and noisy radial current patterns which do not correspond to the main picture of a dipole structure expected for a dominant westwards flowing current vein. The calibrated map is more consistent in this respect.

c. Self-calibration with multiple sources

Whenever several far sources are available, the strong hypothesis of constant phase corrections $\delta\phi_n$ can be relaxed and a dependence on the bearing can be introduced. This is the case for the

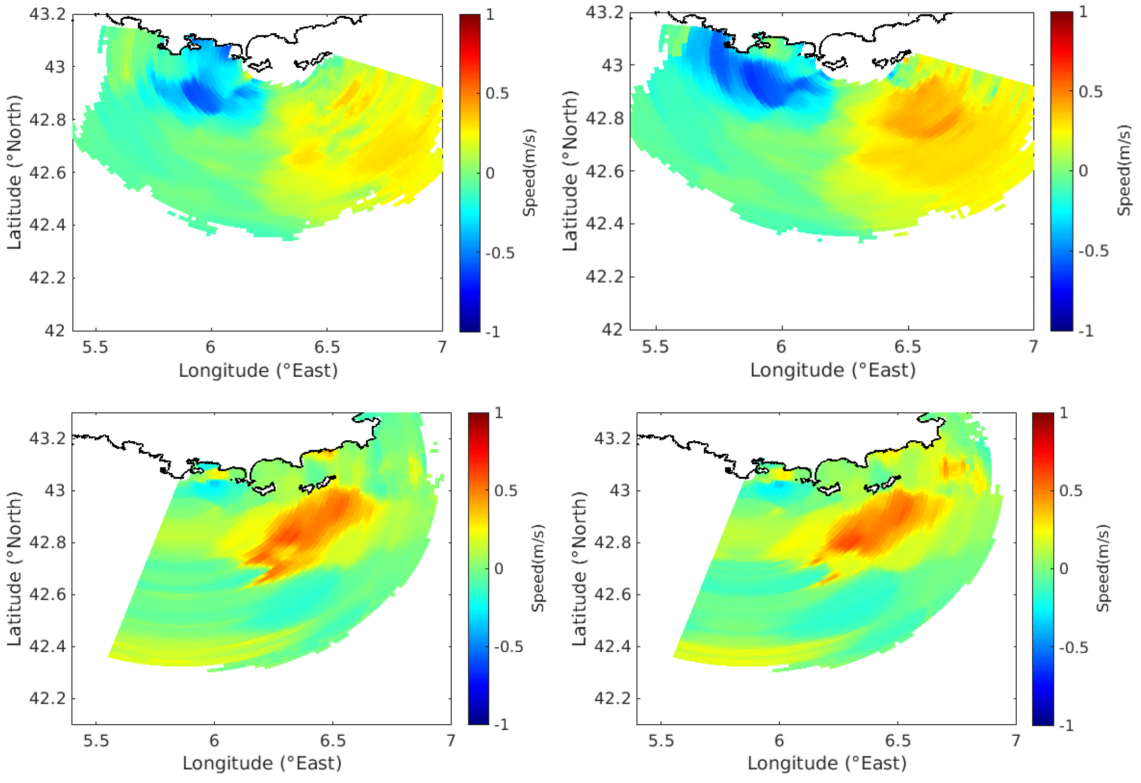

Fig. 4. Top panels: elliptical velocity maps obtained on October 13, 2019, 17.00 UTC from one-hour observation with the Porquerolles transmitter and Cap Bénat receiver. The azimuthal processing of HFR data has been performed using the BF method without (top left panel) and with (top right panel) self-calibration. Bottom panels: radial velocity map obtained on November 11, 2020, 03.00 UTC from one-hour observation with the Peyras transmitter and receiver, without (bottom left panel) or with (bottom right) self-calibration.

multistatic HFR network in Toulon where the two distant emitters (POR and PEY) can be used on the receiver site (BEN). Consider the general situation of M available far sources in directions $\theta_1 \leq .. \leq \theta_M$. The one-source calibration can be generalized by defining the relative phase $\tilde{\phi}_{m,n}$ of the complex direct signal produced by the mth source on the nth antenna:

$$\tilde{\phi}_{m,n} = arg\left(\frac{\tilde{D}_{m,n}}{\tilde{D}_{m,1}}\right) \tag{9}$$

leading to a phase correction:

$$\delta\phi_{m,n} = \tilde{\phi}_{m,n} - \phi_{m,n} \tag{10}$$

A bearing-dependent phase correction $\delta\phi_n(\theta)$ can be obtained by the utilization of the above coefficients in the vicinity of each source direction. To avoid the discontinuity of the phase corrections and to ensure their consistency the prescribed phase corrections (in fact, their sinus and cosinus to avoid phase ambiguity) are interpolated in every angular sector defined by two successive source bearings θ_m and θ_{m+1}. For bearings that are beyond the extreme sources ($\theta \leq \theta_1$ and $\theta \geq \theta_M$) a constant phase correction given by the closest source (θ_1 or θ_M) is assumed.

4. Antenna grouping

a. Direction Finding and its issues

The DF technique is a high-resolution method for determining the directions of arrival (DOA) of unknown sources (also referred to as "emitters" in the literature) in the far field. It is based on the MUSIC (MUltiple SIgnal Classification) algorithm (Bienvenu and Kopp 1983; Schmidt 1986; Krim and Viberg 1996) applied to each complex Doppler ray measured on every single antenna. It allows finding at most $N-1$ DOA by combining N antennas. In the context of surface current mapping, the DOA are the bearings associated with each given value of the radial or elliptical velocity, corresponding to a given Doppler shift. The MUSIC algorithm assumes that the signal originating from the different sources is a discrete, stationary random process (of dimension N) and is perturbed by an additive white random noise vector. The covariance matrix Σ of the complex antenna signals is a $N \times N$ matrix with elements

$$\Sigma_{ij} = \mathrm{Cov}\left(Y_i, Y_j^*\right) \tag{11}$$

where Y_i is the complex Doppler ray (at a given frequency shift) from the ith antenna. To evaluate this quantity, the coherent time series recorded on each antenna channel is split into overlapping intervals and an estimation of the complex Doppler spectrum is obtained for each time interval. This provides for each pair (i, j) of antennas and each Doppler ray a certain number of (quite) independent samples from which the ensemble average in (11) can be evaluated. The optimal number of samples results from a trade-off between the convergence of the matrix cross-products to their statistical mean and the Doppler frequency resolution which decreases with the sample size.

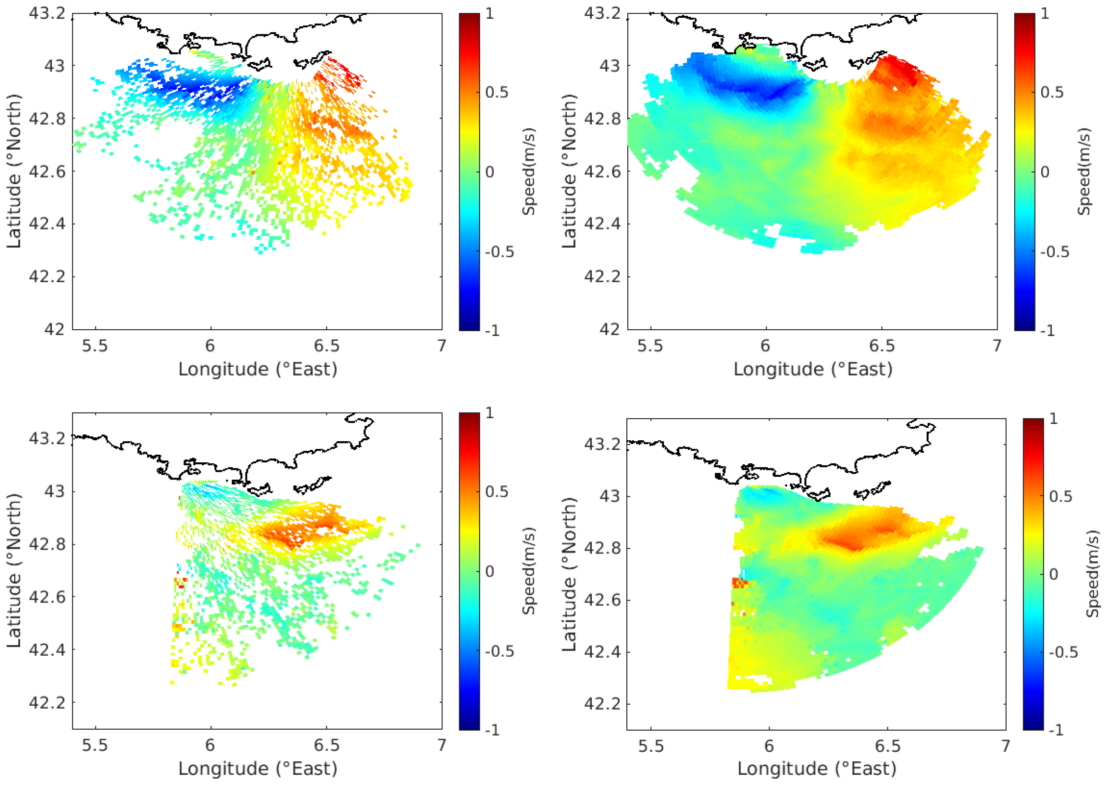

FIG. 5. Elliptical velocity obtained on October 13, 2019, 17.00 UTC from one-hour observation with the Porquerolles transmitter and Cap Bénat receiver. The azimuthal processing of HFR data has been performed using DF azimuthal processing with one single array of 12 antennas (top left panel) and antenna grouping with all subarrays of 8 to 12 antennas (top right panel) and with stacking from 1 to 6 sources with each subarray. The self-calibration of antenna phases has been applied in both cases. Same case with Peyras on November 11, 2020, 03.00 UTC at the bottom.

Next, a Singular Value Decomposition (SVD) of the covariance is sought, $\Sigma = U\Lambda U^*$ where $\Lambda = \mathrm{Diag}(\lambda_1, ..., \lambda_N)$ is the diagonal matrix of singular values ($\lambda_1 \geq ... \geq \lambda_N \geq 0$) and $U = (\boldsymbol{U}_1, ..., \boldsymbol{U}_N)$ is the matrix of eigenvectors $\boldsymbol{U}_j$. In the absence of noise, the M positive singular values $\lambda_1 \geq .. \geq \lambda_M > 0$ identify the number and strength of the different sources and the associated eigenvectors $\boldsymbol{U}_1, .., \boldsymbol{U}_M$ their direction. Precisely, the eigenvectors coincide with the normalized steering vector in the direction θ_j of the source, $\boldsymbol{U}_j = \boldsymbol{a}(\theta_j)/\left\|\boldsymbol{a}(\theta_j)\right\|$. The remaining $N - M$ eigenvalues $\lambda_{M+1} = .. = \lambda_N = 0$ and associated eigenvectors $\boldsymbol{U}_{M+1}..\boldsymbol{U}_N$ define the null subspace. In the presence of noise, these last eigenvalues are nonzero but are supposed to be lower than the signal eigenvalues

($\lambda_N \leq .. \leq \lambda_{M+1} << \lambda_M$); the corresponding subspace is called the noise subspace. The idea of the MUSIC algorithm is to identify the direction of arrival by minimizing the projection of the steering vector onto the noise subspace, which amounts to maximizing its inverse:

$$Q(\theta) = \frac{||\boldsymbol{a}(\theta)||^2}{||\sum_{m=M+1}^{N}[\boldsymbol{a}(\theta)\cdot\boldsymbol{U}_m^*]\boldsymbol{U}_m||^2} \tag{12}$$

This quantity is referred to as the MUSIC DOA function; its first M maxima above some threshold identify the sources. As it is well-known, the main advantage of the DF method with respect to the BF method is its better ability to detect sharp spatial variations of surface current and the better robustness of its estimates to decreasing Signal-to-Noise Ratio (SNR) and increasing bearing angles (Laws et al. (2000)). However, there is no plain definition of azimuthal resolution in that case and statistical quantification based on the uncertainty of the DOA must be devised to replace this concept (Emery and Washburn (2019)), wherein the size of the antenna array implicitly plays an important role.

The left panel in Figure 5 shows an example of elliptical velocities obtained with the Porquerolles - Cap Bénat pair on the same dates. The range-resolved time series have been processed with DF using the full array (12 antennas) assuming 3 sources and using the same radial grid as for BF processing (1.5 km $\times$ 1 degree). As expected, the DF processing leads to current maps with sharper contrasts and a gappy structure while BF smoothes out the small current patterns. For such high-resolution maps with small angular steps, many bearings are either not identified or do not pass the MUSIC thresholds, leaving blank areas. Increasing the filling ratio can in general only be realized at the expense of accuracy and a trade-off between these two requirements must be found with the setting of the DF parameters. As seen in the next section, antenna grouping is a way to optimize the filling ratios without reducing the thresholds.

b. Antenna grouping

Except for rare exceptions (Wang and Gill 2016; Kirincich et al. 2019), high-resolution techniques are employed with compact systems having a small number of antennas (typically 3, as for the SeaSonde CODAR) while the BF techniques are used with extended arrays of at least 8 antennas. Using DF processing with large antenna arrays open new possibilities which are not permitted by compact systems. A major improvement to prevent the lacunarity of radial or elliptical surface

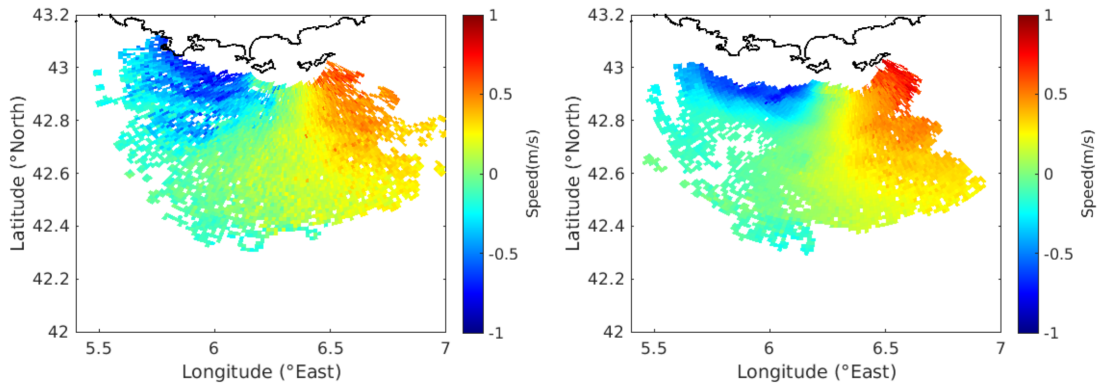

305 FIG. 6. Same case as Figure 5 with DF azimuthal processing using 10 admissible subarrays of 3 antennas with
306 (left panel) and without (right panel) self-calibration

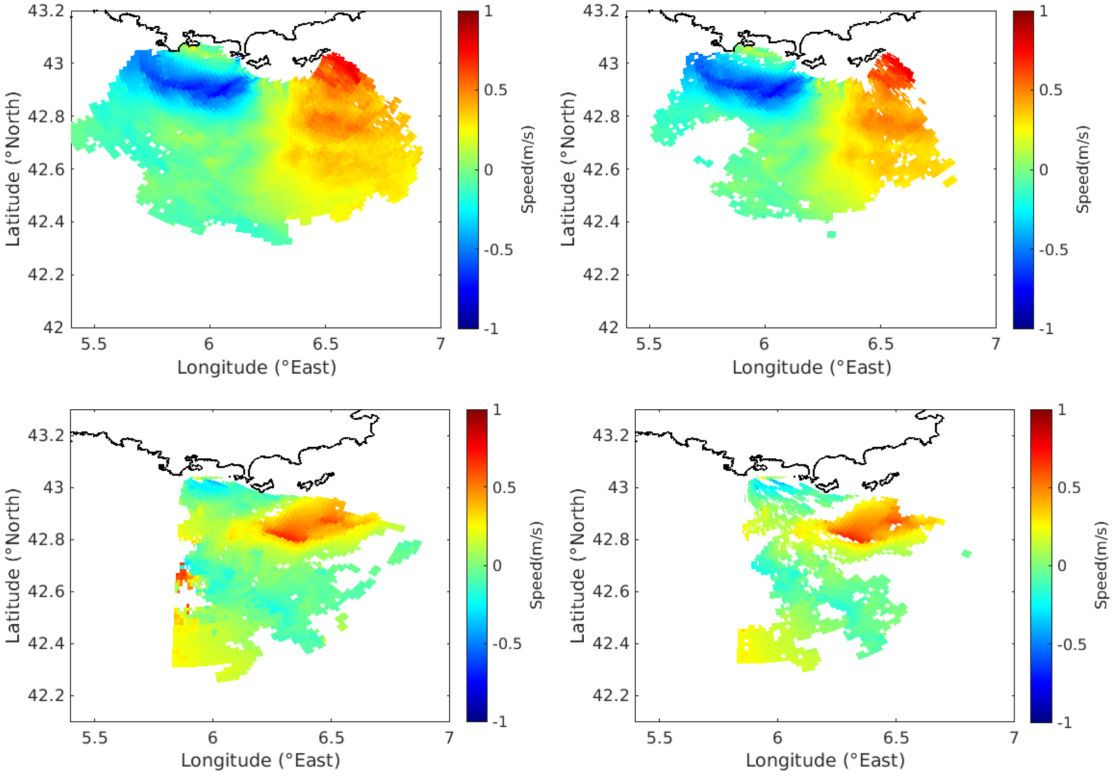

307 FIG. 7. Same case as Figure 5 with DF azimuthal processing using antenna grouping with all subarrays of 4
308 to 12 antennas whenever 1 antenna (number 7, top left panel) or 3 antennas (number 3,7 and 8, top right panel)
309 in the array are out of service. Same case with Peyras at the bottom.

current maps is to extend the DF processing to all possible combinations of subarrays made of consecutive antennas, a method that will be referred to as "antenna grouping". Instead of restricting the covariance analysis to a single maximal set of antennas, it can be applied as many times as there are admissible subarrays of arbitrary size. The idea of using subarrays in DF is not completely new as it is a well-known method (see the review in (Krim and Viberg 1996)) to improve the estimation of the covariance matrix at the cost of a reduction of the signal subspace dimension. However, one can take advantage of subarrays differently, as they can be used to obtain many independent estimations of elliptical velocities and can be allowed an arbitrary size, from a minimal N_{min} to a maximal size N corresponding to the length of the full array. It is simple combinatorics to see that there are $(N-N_{min}+1)(N-N_{min}+2)/2$ such subarrays. The idea is to perform a weighted mean of elliptical velocities obtained with the different subsets of antennas, by averaging all the elliptical velocities falling into each bin of bearing. As they are many subarrays, this increases considerably the probability of visiting a given radar cell (that is, one range and one bearing) with the DF algorithm. In fact, most bearings will be visited several times while looping over the subarrays, with possibly different values of the elliptical velocity (that is, possibly distinct Doppler rays). This improves the filling of the map and also provides more reliable and accurate estimates of elliptical velocities with fewer outliers. A quality check is performed by rejecting the azimuthal bins inside which the standard deviation of velocities is too large (> 20 cm/s in our case). Smaller groups of antennas have in principle a coarser azimuthal resolution than larger groups. As a result, they are less accurate to evaluate the surface elliptical velocity because they tend to smooth the latter. In addition, they are limited to a small number of sources with the effect that they can miss some specific features of the surface current pattern in case of complex meandering structures. However, they are more robust to noise and have a better filling factor. On the other hand, larger groups have an increased azimuthal resolution and accuracy and allow for a larger number of sources but are more lacunary. These complementary strengths and weaknesses of small and large antenna groups compensate each other when the outcome of all possible subarrays is averaged. A stronger weight is attributed to the current estimated with large antenna groups which are sparser but more accurate. At this stage of the discussion, only qualitative considerations will be given regarding the various parameters involved in this improved DF processing; quantitative detailed information will be found in Section d.

The right panel in Figure 5 shows the same map as the left panel, with a weighted mean of the elliptical velocities obtained with a DF process applied to consecutive groups of 8 to 12 antennas with source stacking (see subsection c) from 1 to $4, 5$ or 6 sources depending of the size of the array (85 combinations) with a preliminary complex antenna gain correction with the self-calibration method. The radial grid resolution is unchanged, that is 1.5 km $\times$ 1 degree. A clear increase of the spatial coverage is obtained with almost the same filling ratio as for BF while the surface current patterns appear with finer details and enhanced contrast, a qualitative improvement that will be confirmed quantitatively in Section 6. Note that antenna grouping technique can be applied to monostatic as well as bistatic or multistatic systems.

The key point in using small antenna subarrays is a good preliminary phase calibration which is a requisite for the success of antenna grouping. Whereas a missing or imperfect calibration of complex antenna gains is less visible when performing DF on a long array, it can have a noticeable impact on short arrays since it can produce a small rotation of the elliptical current maps. When averaging the individual elliptical currents obtained with the different short arrays, this can blur the final elliptical velocity map. This artifact can be mitigated with the self-calibration technique which allows correcting the complex antenna gains first inferred from geometrical considerations. To test the efficiency of self-calibration, surface current maps were produced with 10 groups of 3 antennas with and without self-calibration (Figure 6). On the left panel, the effect of individual group rotation is visible in the dispersed blue area at the western end of the domain; after phase correction, the current maps obtained with the different groups have a better overlap and show a clearer pattern of the dipolar radial current.

Besides increased resolution and filling ratio, another interesting performance of the antenna grouping method is its robustness to the failure of some antennas in the array. This is a very valuable quality as it often occurs for various reasons that one or several antennas in the remote receiving sites are out of service (because of e.g. corrosion, damaged individual receiver or connector, vandalism, etc) and cannot be repaired at once. Contrarily to BF, the DF with antenna grouping can still be efficient with an incomplete array, even though the resulting elliptical current maps deteriorate little by little as an increasing number of antennas are missing. Figure 7 shows the same radial current map as in Figure 5 obtained by applying the DF method with antenna grouping to all subarrays of 4 to 12 antennas whenever a certain number of antennas are discarded.

c. Source stacking

In the subspace-based methods for DOA (e.g Krim and Viberg (1996)), the number of sources is defined as the dimension of the signal subspace or, what amounts to the same, the number of non-zero eigenvalues. The complementary subspace with null eigenvalues is referred to as the noise subspace. However, in actual situations with real data, it is difficult to separate unambiguously the zero and non-zero eigenvalues, as a continuum set of decreasing values is obtained after SVD of the covariance matrix with no clear change in the order of magnitude of the latter. This makes the automatic detection of the number of sources quite challenging, even though some theoretical or empirical approaches have been proposed in the literature (e.g. Kirincich et al. (2019)). Given the possibly large number of sources with phased arrays (here, from 1 to 11), there is no obvious choice for the best compromise. Using a low number of sources allows to reduce the false detections in MUSIC peaks and yields smoother, less noisy current maps; it loses, however, some fine structures of the circulation pattern such as meandering, veins of current, or eddies. Increasing the number of sources allows for a faithful rendering of the complex geometrical patterns but is more prone to noise and spurious detection (e.g. Kirincich et al. (2019)). To operate a trade-off between these two constraints, a principle similar to that of the antenna grouping can be employed. The MUSIC algorithm can be applied several times with a varying number of sources and the resulting radial surface currents can be averaged with a weight that depends on the number of sources. This technique will be referred to as "source stacking" as it permits to increase the number of estimations and the spatial coverage by accumulating the results obtained with different number of sources. Source stacking is applied to every sub-array in the antenna grouping procedure. This improves the mapping of complex geometrical current patterns while reducing noise and lacunarity.

d. How should one set the DF parameters ?

They are many required parameters to float to optimize the DF with antenna grouping and source stacking and a quasi-infinite way to do this. We tried to devise an automatic and sufficiently universal way to select them, which was validated in the light of the drifter comparisons (Section 6). If not optimal, this choice has the merit of being reproducible by other users of the oceanic community. The setup of the different parameters is listed hereafter.

1. Setting the limits of the first-order Bragg region in the range-Doppler spectrum is the first important step of the DF processing. The key point is to avoid misinterpreting second-order Bragg lines as first-order peaks (see the detailed discussion in Section 4d and references therein). Dynamical and automatic bounds have been chosed for the first-order region based on the statistical distribution of radial currents. Starting with an absolute maximal value of 1 m/s for the radial current (a threshold that is adapted to the local situation) a preliminary DF analysis is performed at each cycle of processing (that is, every hour) to estimate the distribution of radial currents over the radar coverage. Outliers to the distribution, some of which could be due to misinterpreted second-order Doppler spectra, are removed by restricting the first-order limits to the 99% quantile of the Doppler frequency shifts. The improved DF analysis is then performed with these refined first-order limits.

2. The size N_{sub} of subarrays (i.e. the number of consecutive antennas defining a subgroup) should be as large as possible to preserve accuracy while keeping a sufficient number of possible combinations. With a 12-antenna array, one can retain the sub-arrays of size ≥ 8, leading to 5+4+3+2+1=15 possible groups.

3. To preserve a good contrast of the local maxima of the MUSIC DOA function with respect to secondary peaks, the dimension of the noise subspace should be left as large as possible while preserving the existing sources. A minimal dimension of 3 is imposed for the noise subspace.

4. The number of sources should be sufficiently large to account for all physical sources but one should not create fictitious sources by making this number too high. We found that increasing the number of sources beyond 3 deteriorates the accuracy even if it allows filling the remaining gaps in the current map.

5. The MUSIC thresholds should realize a trade-off between missing detection and false alarms. Their magnitude depends on the size of the group and the dimension of the noise subspace. To make an automatic adjustment of the threshold, the statistical distribution of values of the MUSIC DOA function was evaluated by looping over all range-Doppler cells for a given size of group and number of sources. The “big” factors corresponding to the actual MUSIC maxima are identified by a percentile of the distribution multiplied by a scaling factor (which generalizes the usual 2 standard deviation criterion for Gaussian distributions). We found

empirically that the threshold should be set to 1.8 times the 72th percentile of the MUSIC DOA function.

6. The weights $w_{N_{sub},M}$ of the subarrays should favor the largest arrays and the number of sources smaller than 4, with damping of higher sources more pronounced for the smallest arrays. The following empirical formula was found to work for 12 and 16 antenna arrays:

$$w_{N_{sub},M} = 1.3^{N_{sub}} \exp\left(-2\frac{(M - N_{sub}/9)^4}{(2N_{sub} - 3)^2}\right) \tag{13}$$

5. Denoising

a. The different types of noise

The main limitation of surface current mapping is the presence of noise on the antenna signals, which deteriorates both the range and the accuracy of the estimation. While external sources of noise can in general not be removed, their impact can be mitigated by adequate signal processing techniques. There are 3 types of parasitic external noise, which must be handled with different techniques. The first source of external noise is the interference of external emitters in neighboring frequency bands. These are commonly referred to as Radio Frequency Interferences (RFI). Their characteristic signature is a vertical strip in the range-Doppler representation (Figure 8a) and the contamination of an entire azimuthal sector in the radial maps (8b). The second type of noise originates from the ship echoes (Gurgel and Schlick 2005). Whenever a vessel crosses a radar cell with a radial speed of the same order of magnitude as the surface current, it produces a bright spot around the corresponding location in the range-Doppler map. Figure 8c shows an example of a range-Doppler map with many presumable ship echoes between the 2 first-order Bragg rays. Figure 8d shows a typical artifact of a ship echo in the radial current map, here an intense outlier (red spot) in the central region. The third type of parasitic signal is the sea surface echo itself when taken at second-order. In the omnidirectional Doppler spectra, the first-order Bragg peaks are broadened by the variation of the radial currents over the radar coverage and can overlap the second-order components of the Doppler spectrum. Figure 8e shows an example of strong second-order echoes overlapping the first-order rays. This results in erroneous spots of various sizes and intensities on the radial map, here a cyan spot in the upper left region of the radial map (Figure 8f).

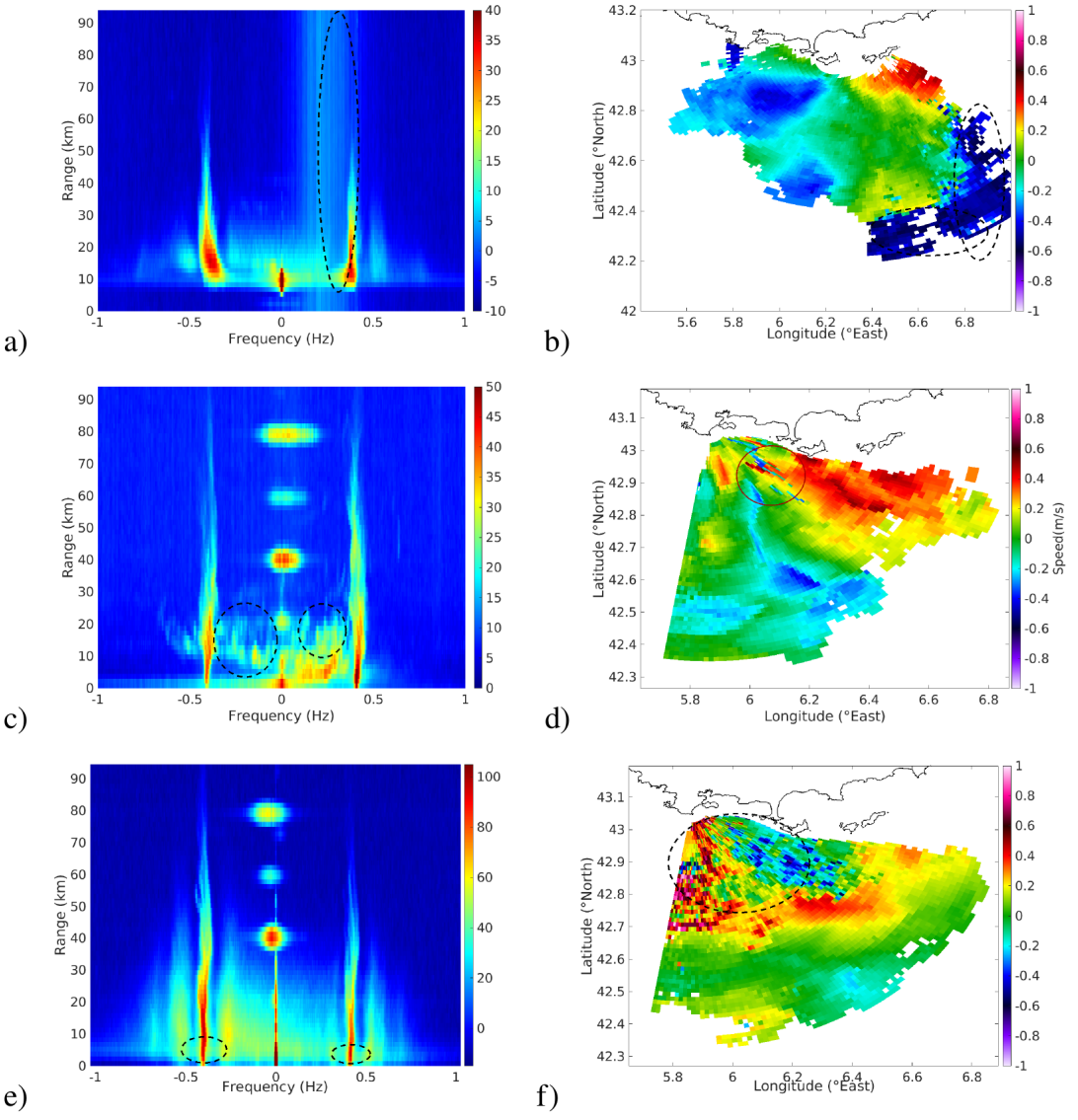

FIG. 8. Range-Doppler spectra (a, c and e) and associated radial maps (b, d and f) illustrating the 3 types of parasitic signals that deteriorate the surface current estimation. The effect of noise is highlighted with the black dashed ellipses. The vertical RFI strips seen on the range-Doppler spectrum from the Bénat receiver (a) produce an erroneous estimation of the elliptical velocity in the Eastern part of the map (b); ship echoes seen as cyan spots inside the Bragg region produce numerous artifacts on the Peyras radial map (d) ; second-order echoes in the vicinity of first-order Bragg rays (d) contaminate the shorter ranges of the Peyras radial map (f). The color scale is given in dB for the spectra and in m/s for the radial speeds.

Judging from the observed statistics at the Toulon HFR network, RFIs are the most frequent and problematic noise (on average 2 hours at specific periods of the day) while ship pollution is sparser in time and space even if it occurs every day. The perturbation induced by second-order echoes is less frequent as it is bound to strong sea states and large currents. In this section, an ensemble of simple methods is proposed for mitigating the aforementioned three types of noise. They are mostly based on appropriate threshold criteria and therefore possibly close to the standard practice of users and manufacturers. However, such techniques are rarely detailed in the literature and we found it important to provide a full quantitative description that makes them reproducible.

b. RFI removal

There exists a wealth of techniques in the radar literature for RFI removal in the context of phased-array oceanographic radars. Many authors use orthogonal subspace methods to cancel the noise interferences (e.g. (Zhou et al. 2005; Zhou and Wen 2012; Chen et al. 2018a)) or Complex Empirical Mode Decomposition (e.g. (Chen et al. 2018b; Nazari et al. 2019)). These methods have been shown efficient but are somewhat complex to apply and require some a priori assumption on the mathematical description of the parasitic signal. Other techniques consist in combining the radar signal with the sea echo removed with the original radar signal including the echoes; this is routinely done with the WERA radar, where the FFT-based range gating process allows to store the echo-free signal corresponding to negative range cell (the so-called ".RFI" files). This technique is well performing and is implemented in commercial software (Gurgel et al. (2007); Gurgel and Schlick (2009)) but requires an extra amount of storage and processing. Here a simple empirical and versatile method is proposed, based on threshold criteria for the far-range Doppler spectrum.

The vast majority of RFI display a characteristic structure in the range-Doppler map, namely they exhibit range-invariant vertical strips. They can thus be easily identified and removed by checking the few farthest range cells for each Doppler bin. Let us denote $\hat{X}(f,d)$ the complex Doppler spectrum at frequency f and range d and $R(f)$ the average power of the Doppler spectrum at frequency f in the last few range cells (that is, those ranges that fall beyond the maximum excursion of Bragg rays). A valid Doppler bin is qualified with a simple 3 dB SNR criterion, that is requiring $\left|\hat{X}(f,d)\right|^2 > 2R(f)$, otherwise the corresponding spectral line is considered as either

RFI or noise and is rejected. Figure 11a illustrates the RFI removal from the elliptical velocity map in Figure 8a.

c. Removal of ship echoes

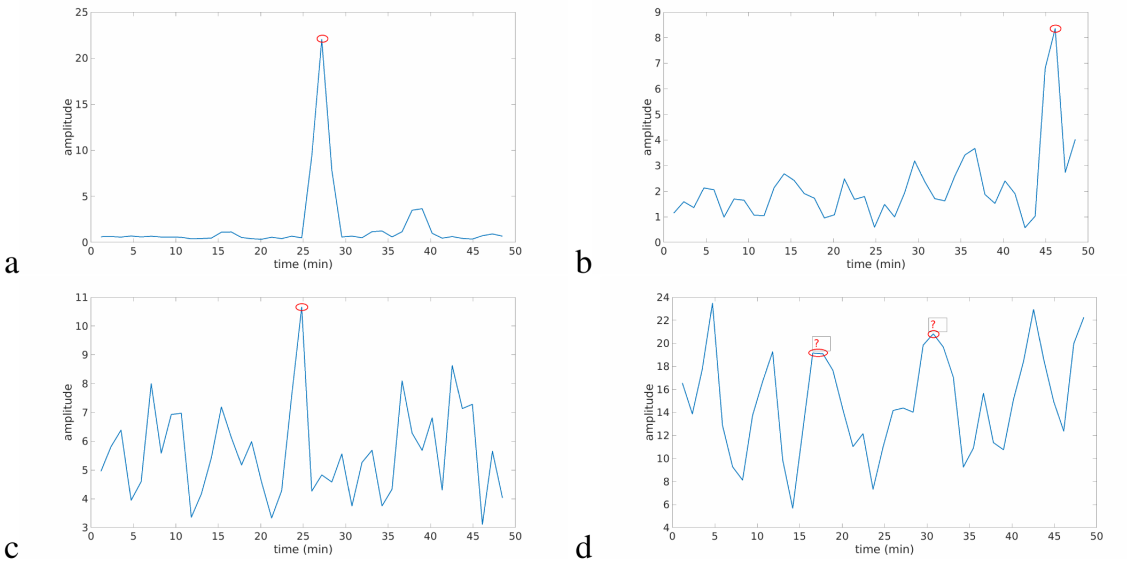

FIG. 9. Times series of the amplitude of Doppler spectrum at 4 distinct locations in the radar-Doppler map indicated in Figure 10. a) A cell in the background noise with a presumable ship echo (circled in red); b) A cell with a weak Bragg signal and a strong ship-like echo; c) A cell with a strong Bragg signal and a slightly stronger ship-like echo; d) A cell with equally strong sea and ship echoes that cannot be discriminated.

The ship echoes are due to the strong backscattered signal from boats or floating objects. In the range-Doppler maps they cause well-localized bright spots around one or several range-frequency cells and this specific structure allows for their identification (Gurgel and Schlick (2005); Gurgel et al. (2011)). The location of the ship echoes in the range-Doppler map varies in time as both the position and radial speed of the ship change. In general, the integration time is much longer that the travel time of a ship through a given radar cell. As the MUSIC DF procedure requires the calculation of a large number of sub-spectra within the integration time (typically one hour), it will be jeopardized by the few samples that have been contaminated by the ship echoes. The spoiled samples can be easily identified through a strong amplitude peak in the time series of sub-spectra at a given range-frequency cell. This is exemplified in Figure 9, where the sub-spectra have been

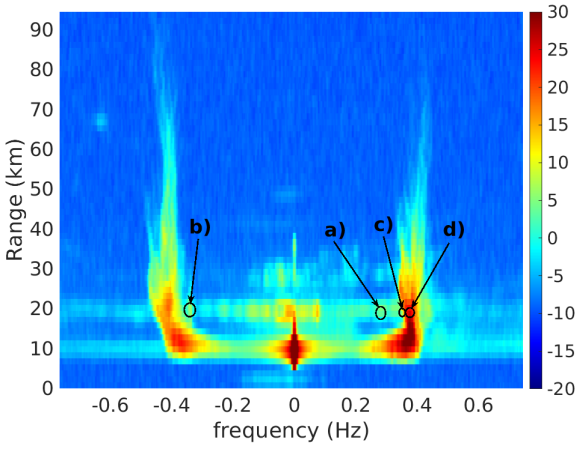

FIG. 10. An instantaneous Range-Doppler spectrum used in the time series of Figure 9. The 4 different test cells are labeled from a) to d).

calculated by using 75% overlapping sliding time intervals of 6 min; they are removed before application of the DF processing. The effect of ship echoes removal is illustrated in Figure 11b.

There are, however, some critical but rare cases where ship echo removal is not possible. The method fails in the instances where the ship echo and the first-order Bragg peak have close locations and magnitude in the range-Doppler map, in which case they cannot be distinguished from one another. The different cases that can be encountered are illustrated in Figure 9, where very likely ship echoes have been identified (even though they could not be certified with AIS or other external information) with increasing level of criticality from a) to d), corresponding to different locations in the range-Doppler map as seen in Figure 10. The sub-figure a) shows the easiest situation of a ship crossing a range-Doppler cell in the background noise with unambiguous identification of the corresponding echo at the time stamp between 25 and 30 min. The second situation b) shows the case of a weak sea echo mixed with a strong ship echo at about 45 min which is still clearly identified. Situation c) is close to critical as the ship echo dominates the sea echo by a smaller amount and thus requires a more stringent test for elimination (that could possibly cause a false-positive). The sub-figure d) shows an instance of the critical case, where ship and Bragg echos cannot be separated. Hence, it is possible to eliminate most of the ship echoes, except for those corresponding to the critical situation d). When establishing a threshold for ship echo identification in the Doppler spectra, a trade-off must be found as usual between the probability of detection and

the probability of false alarm (in which case sea echos are eliminated). We chose and checked empirically a threshold equal to twice the median value of the time series of spectral amplitude at the range-Doppler cell.

d. Removal of second-order sea echoes

The second-order sea echoes are caused by the swell and wind waves. In general the first- and second-order echoes are well separated by a minimum in the omnidirectional Doppler spectrum and can thus be clearly identified. Classical limits for the first-order region rely on the position of a "null" (that is, a minimum) in the Doppler spectrum (see e.g. Lipa and Barrick (1983); CODAR (2002)). However, in the case of rough seas and/or strong currents, second-order peaks may overlap the first-order Bragg region and can be misinterpreted in terms of surface currents. To overcome this effect refined methods based on image segmentation techniques have been recently proposed (Kirincich 2017) and shown to improve the detection of the first-order region with a small number of parameters to tune. Here a simple alternative method is proposed for the elimination of spurious second-order frequencies that does not require any image processing toolbox. It is based on the fact that second-order peaks are usually much weaker than first-order peaks and can be removed using an appropriate threshold criterion. To do this, the mean level of second-order rays is estimated in each range cell d of the omnidirectional Doppler spectrum by averaging the latter in a narrow frequency region at the border of the first-order Bragg frequency search domain (a typical interval of width 0.05 Hz is used) leading to a reference value $B_2(d)$. In a similar way to RFI mitigation, the spectral rays in the first-order Bragg region are compared with this reference value. For ratios smaller than a given threshold (here 3 dB), they are interpreted as second-order and discarded in the DF azimuthal processing. Figure 11c shows the result of second-order artifacts mitigation on the radial current map from Figure 8f. As seen, some residual errors remain but most of the second-order contributions have been eliminated. In setting the threshold, a trade-off must be found between the complete removal of second-order and the loss of "true" first-order contributions.

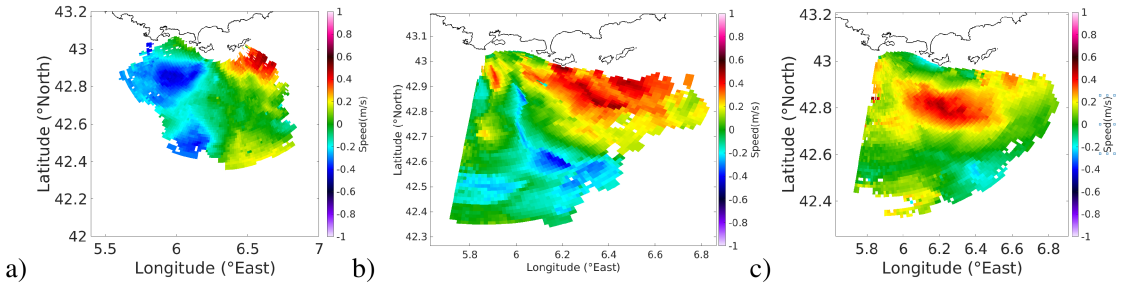

555 FIG. 11. Radial maps from Figure 8 after application of the 3 different techniques for mitigating the noise from
556 a) RFI ; b) ship echoes; c) second-order echoes.

557 6. Performance assessment with drifters

558 *a. The impact of self-calibration*

559 The traditional method to assess the performances of HFR surface current measurement is to
560 perform a comparison with in situ data such as ADCP and drifters (e.g. Graber et al. (1997); Essen
561 et al. (2000); Ohlmann and et. al (2007); Parks et al. (2009); Kalampokis et al. (2016); Kirincich
562 et al. (2019)). As it is well known, these comparisons are made difficult by the differences in the
563 involved spatial and temporal scales (Rypina et al. (2014)), the measurement depth (Sentchev et al.
564 (2017); Dumas et al. (2020)) and the Lagrangian or Eulerian viewpoints (Röhrs et al. (2015)).
565 Nevertheless, the best comparisons achieve RMS differences for the hourly radial current of a few
566 cm/s (e.g. Ohlmann and et. al (2007); Shay et al. (2007); Liu et al. (2014)) while most frequently
567 the obtained RMS difference is of the order of 10-20 cm/s. Note that the difference between HFR
568 and in situ data depends on many other factors such as the sea state (Wei et al. (2020)), the absolute
569 magnitude of currents, or the radar cells that are selected for the comparison or the antenna pattern
570 calibration (Kohut and Glenn 2003; Kalampokis et al. 2016). It follows that a fair comparison
571 between any 2 different signal processing methods can only be performed using the same hardware
572 and the same data. Here, the accuracy of radar-based surface currents will be evaluated, depending
573 on whether they are obtained by BF or DF azimuthal processing, whether or not the self-calibration
574 is applied, and whether or not antenna grouping and source stacking are employed.

578 In an earlier work (Dumas et al. (2020)), a first evaluation of the performances of the HFR
579 network in Toulon was made using the newly developed processing methods (self-calibration and

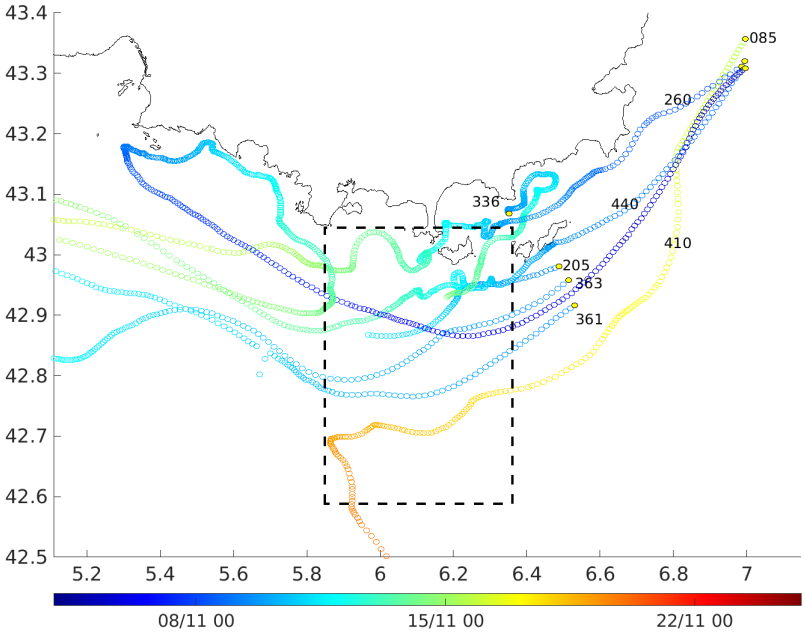

FIG. 12. Drifter trajectories during the November 2020 campaign. 4 drifters were launched on November 9, off the Levant islands (drifters 205, 336, 361,363), 4 others came from Italy from an earlier launch (drifters 85, 260, 410,440). The black dashed box shows the approximate radar coverage.

antenna grouping). At that time, the source stacking, multi-source calibration, and noise mitigation were not availaible and the methodological aspects of the DF processing were not discussed. The CARTHE drifters (Novelli et al. (2017)) were shown to be very relevant to assess the performances of HFR measurements in the near- and mid-range of the radar coverage, with only a few cm/s RMSD in comparison with the radar-derived radial velocities. They integrate the current over a depth of 65 cm which is close to the effective integration depth of the HFR at 16.15 MHz ($\lambda/8\pi$ = 74 cm). Here, another original campaign with the same kind of drifters is used to assess specifically the performances of the improved HFR data processing and its parametrization. The test area has been chosen wider and farther off the coast with some trajectories crossing the southern limit of the radar coverage. A launch of 4 drifters was realized on November 9, 2020, south of the Levant island in the easternmost region of the radar coverage, along a latitudinal section (43°N). This deployment strategy was dictated by the desire to target Northern Current and thus have trajectories traveling westward through the radar coverage. In addition, a cluster of 20 drifters was deployed

in the open sea area in front of Livorno (Italy) by our Italian colleagues from CNR one month earlier (Berta et al. (2021)) and some of the drifters reached our area of interest. Combining this opportunity experiment with our local experiment, a total of 8 drifters have crossed the radar coverage in the period 9-12 November, some of them leaving and reentering the observation zone such as the drifters 410 or 440, as shown in Figure 12.

The surface currents measured by the drifters were projected onto the local radial and elliptical directions in order to be compared with the measurement of the corresponding surface current component with the monostatic (Peyras) and bistatic (Bénat) HFR stations. To evaluate the performances of the multiple source calibration, the elliptic velocity inferred from the bistatic receiver in Bénat was calculated with either no external calibration, one single-source calibration (with the Porquerolles or Peyras transmitter), or 2-source calibration (with the Porquerolles and Peyras transmitters); similarly, the radial velocity inferred from the monostatic receiver in Peyras was calculated with either no external calibration or one single-source calibration with the Porquerolles transmitter. The antenna grouping and source stacking techniques were further employed to increase the spatial coverage as described in Section b, with a choice of the DF parameters along the guidelines of subsection d. The measurements along the 8 drifter trajectories and the corresponding HFR estimations were stacked together and the global Root Mean Square Difference (RMSD) between the in situ and HFR velocities was calculated along with the correlation coefficient. The results are summarized in Table 1. The use of the self-calibration shows a clear improvement in the accuracy, especially for the Peyras station where a reduction of about 2 cm/s is obtained for the RMSD. Similarly, the use of the 2-source calibration yields slightly more accurate results than with one single source.

b. The impact of antenna grouping and source stacking

The respective performances of antenna grouping and source stacking compared to the classical MUSIC analysis were established with the bistatic Bénat receiver by calculating the RMSD of drifters/HFR velocities as well as the resulting spatial coverage of surface currents. The latter is defined as the percentage of successful surface current estimations on the range-azimuth grid, which extends over 64 range bins (96 km) and 166 azimuthal bins (from 174 to 340 degrees CCW from East). The DF estimation of surface velocities from the Bénat bistatic receiver with

	Peyras		Bénat	
	RMSD	Corr	RMSD	Corr
No calib.	9.5	0.89	10.1	0.90
POR	7.6	0.93	8.9	0.92
PEY	N/A	N/A	8.7	0.92
POR/PEY	N/A	N/A	8.2	0.93

TABLE 1. Statistical comparison between the HFR radial velocities measured from the Peyras and Bénat stations and measured from the drifters. The azimuthal processing has been performed with DF using antenna grouping and different modes of self-calibration: no calibration, calibration with the Porquerolles transmitter (POR), the Peyras transmitter (PEY), or both (PEY/POR). The last two calibration modes are not applicable (N/A) to the Peyras station. The Root Mean Square Difference (RMSD) is given in cm/s.

and without antenna grouping has been performed for a fixed number of sources ranging from 1 to 6 as well as with source stacking. Subarrays of size ≥ 8 have been considered and other DF parameters have been set along the lines of subsection d. The results are summarized in Table 2. As seen, increasing the number of sources beyond 4 deteriorates the accuracy but does not significantly increase the coverage. Adding antenna grouping increases the accuracy by about $10-20\%$ and makes the coverage almost twice as large. Note that the poor performance of the 1-source estimation (12.1 cm/s RMSD) is mitigated by the antenna grouping technique (8.8 cm/s) which can eliminate outliers in averaging the estimations of subarrays DF. The best performance in all respects is achieved with combined source stacking and antenna grouping techniques.

c. DF versus BF

The reference of the drifter measurement allows for quantitative comparisons of the respective performances of the BF and DF processing. As it is well known, both techniques have their advantages and shortcomings (Laws et al. 2000). The BF yields a larger coverage with fewer outliers but has a tendency to smooth the maps and diminish the contrast; it is therefore not adapted to describe sharp fronts of currents. The DF can produce a higher level of detail but suffers from lacunary estimation and frequent outliers. However, as these methods are in general designed for different types of antenna arrays (compact arrays with DF and extended linear arrays with BF), there are only a few benchmarks of the 2 techniques in the literature. To our best knowledge, this

# sources	grouping	RMSD (cm/s)	Corr	Coverage (%)
1	without	12.1	0.82	9.9
2	without	10.7	0.85	15.5
3	without	10.8	0.85	19.0
4	without	10.7	0.85	21.3
5	without	10.9	0.86	22.6
6	without	10.9	0.86	23.8
1	with	8.8	0.92	25.6
2	with	8.3	0.93	35.6
3	with	9.0	0.91	40.5
4	with	9.3	0.91	43.7
5	with	9.5	0.90	43.7
6	with	9.6	0.90	42.7
sources stacking	with	8.2	0.93	45.5

TABLE 2. Performances of HFR surface velocities estimation from the bistatic Bénat receiver when compared to drifters velocities. The DF calculation is performed with a fixed number of sources without (upper half of the table) and with (lower half of the table) antenna grouping. The last line shows the simultaneous performance of source stacking (for 1 to 6) and antenna grouping.

has only been done in (Wang and Gill 2016), who performed such a comparison with an 8-antenna array and concluded that the DF is slightly more accurate with a relative RMSD reduction of 0.8 cm/s. Here, this idea is pursued by comparing the radial and elliptical surface currents estimated with either BF or DF azimuthal processing on the 12-antenna arrays and by taking advantage of the antenna grouping method, which mitigates the main defaults of the latter (that is, strong lacunarity and outliers). Note that our receive arrays illustrate both the monostatic (Peyras) and bistatic (Bénat) configuration. To make a fair comparison, the same self-calibration has been applied before processing and the same angular mask has been employed to ignore the regions with poor SNR in the shadow of islands. The angular resolution of BF deteriorates by a factor of 2 at a steering direction of 60 degrees away from the normal to the array. Therefore, an extra calculation was made inside the ± 60 degrees receiving angle to evaluate the BF in appropriate conditions. The results of the statistical comparison with drifter's are summarized in Table 3. A significant improvement of the RMSD and the correlation coefficient is obtained with the DF

	Peyras		Bénat	
	RMSD	Corr	RMSD	Corr
DF	7.6	0.93	8.2	0.93
BF deg	9.9	0.86	15.8	0.72
DF $\|\theta\| < 60$ deg	7.6	0.92	8.1	0.93
BF $\|\theta\| < 60$ deg	9.2	0.86	11.2	0.85

TABLE 3. Respective statistical performances of the BF and DF azimuthal processing (with antenna grouping and self-calibration) for the monostatic (Peyras) and bistatic (Bénat) receive stations when compared to the drifters measurements. The Root Mean Square Difference (RMSD) is given in cm/s. The results are given for the full radar coverage (with a land mask) and for a restricted angular opening $\theta < 60$ degrees.

method as compared to the BF method. Note that the amelioration is more pronounced with the Bénat station than with the Peyras station. The reason is that the orientation of the antenna array in Peyras is optimal to cover the NC in the Eastern direction, where most of the trajectories lie. This is optimal for the resolution of the BF method, which is here employed at small incidence angles. Nevertheless, the BF method is still outperformed by the DF method even in these optimal conditions.

7. Conclusion

We have presented a series of techniques that improves the "voltage to current" processing chain for phased-array oceanographic radars. They mostly address the azimuthal processing of sea surface echoes for surface current mapping; at the same time, some simple and efficient empirical solutions have been proposed to mitigate the impact of noise.

Range-resolved complex time series on each antenna are obtained by fast-time Fourier transform of the radar signal within each chirp duration and a self-calibration is then operated on range-resolved time series on the antenna array. A slow-time Fourier transform at the chirp rate is applied to yield the omnidirectional Doppler spectra. These individual antenna spectra undergo a denoising procedure before being combined in a DF analysis with the aforementioned improvements (antenna grouping and source stacking). In the end, this leads to high-resolution surface current maps. Quantitative comparisons with drifter measurements have shown the gain in accuracy that can be obtained with this ensemble of techniques. A comparison has also been made with the

traditional BF method and has shown a global increase in accuracy and enhanced capabilities with respect to this last method.

We hope that these novel processing techniques will be useful to other HFR oceanographic networks. Preliminary results with the phased-array HFR systems in Normandy (Lopez et al. 2020) and in the Golf of Trieste (Querin et al. 2021) have shown promising results. Another benefit of the improved DF processing is that it no longer requires post-processing of surface current maps that is usually done to fill the gaps and clean up the outliers. At this stage, the performances of antenna grouping and optimal interpolation were not compared but we believe that this will be beneficial in the case of big spatial gaps. Elucidating this point is left for future research.

Acknowledgments. Part of this work was issued as an ArXiv preprint (Dumas and Guérin (2020)) to benefit from the feedback of the scientific community. Many thanks go to Anne Molcard for sharing and helping with the drifter's data. This work has been partly supported by the EU Interreg Marittimo projects SICOMAR-PLUS and SINAPSI. We acknowledge the MOOSE program (Mediterranean Ocean Observing System for the Environment) coordinated by CNRS-INSU and the Research Infrastructure ILICO (CNRS-IFREMER). We thank the Parc National de Port-Cros (PNPC) for its support and hosting of our radar transmitter in Porquerolles Island. We also thank the "Association Syndicale des Propriétaires du Cap Bénat" (ASPCB) for allowing our receiver array at the Cap Bénat as well as the Group Military Conservation and the Marine Nationale for hosting our radar installation in Fort Peyras.

Data availability statement. Data are available on demand.

References

Balanis, C. A., 2016: *Antenna theory: analysis and design*. John wiley & sons.

Barbin, Y., 2011: High Resolution Surface Currents Mapping using Direction Finding Method in Bistatic Radar Configuration. *Third Conference on Remote Ocean Sensing*, La Spezia, Italy, URL https://hal.archives-ouvertes.fr/hal-00745299.

Barbin, Y., P. Broche, and P. Forget, 2009: High Resolution Azimutal Radial Current Mapping with Multisource Capability. *Radio Oceanography Workshop 2009*, Split, Croatia, URL https://hal.archives-ouvertes.fr/hal-00745359.

Barrick, D. E., 1972: Remote sensing of sea state by radar. *Engineering in the Ocean Environment, Ocean 72-IEEE International Conference on*, IEEE, 186–192.

Berta, M., P.-M. Poulain, R. Sciascia, A. Griffa, and M. Magaldi, 2021: Carthe drifters deployment within the ddr20. drifter demonstration and research 2020" experiment in the NW Mediterranean sea. Tech. rep., SEANOE, https://doi.org/10.17882/85161.

Bienvenu, G., and L. Kopp, 1983: Optimality of high resolution array processing using the eigensystem approach. *IEEE Transactions on acoustics, speech, and signal processing*, **31 (5)**, 1235–1248.

Chen, Z., F. Xie, C. Zhao, and C. He, 2018a: An orthogonal projection algorithm to suppress interference in high-frequency surface wave radar. *Remote Sensing*, **10 (3)**, 403.

Chen, Z., F. Xie, C. Zhao, and C. He, 2018b: Radio frequency interference mitigation for high-frequency surface wave radar. *IEEE Geoscience and Remote Sensing Letters*, **15 (7)**, 986–990.

CODAR 2002: Technical Codar Support. Defining first-order region boundaries. URL http://support.codar.com/Technicians_Information_Page_for_SeaSondes/Docs/Informative/FirstOrder_Settings.pdf.

Crombie, D. D., 1955: Doppler spectrum of sea echo at 13.56 mc./s. *Nature*, **175 (4459)**, 681–682.

Dumas, D., A. Gramoullé, C.-A. Guérin, A. Molcard, Y. Ourmières, and B. Zakardjian, 2020: Multistatic estimation of high-frequency radar surface currents in the region of toulon. *Ocean Dynamics*, **70 (12)**, 1485–1503.

Dumas, D., and C.-A. Guérin, 2020: Self-calibration and antenna grouping for bistatic oceanographic High-Frequency radars. arXiv, URL https://arxiv.org/abs/2005.10528.

Emery, B., and L. Washburn, 2019: Uncertainty estimates for SeaSonde HF radar ocean current observations. *Journal of Atmospheric and Oceanic Technology*, **36 (2)**, 231–247.

Emery, B. M., L. Washburn, C. Whelan, D. Barrick, and J. Harlan, 2014: Measuring antenna patterns for ocean surface current hf radars with ships of opportunity. *Journal of Atmospheric and Oceanic Technology*, **31 (7)**, 1564–1582.

Essen, H.-H., K.-W. Gurgel, and T. Schlick, 2000: On the accuracy of current measurements by means of HF radar. *IEEE Journal of Oceanic Engineering*, **25 (4)**, 472–480.

Fernandez, D. M., J. Vesecky, and C. Teague, 2003: Calibration of hf radar systems with ships of opportunity. *IGARSS 2003. 2003 IEEE International Geoscience and Remote Sensing Symposium. Proceedings (IEEE Cat. No. 03CH37477)*, IEEE, Vol. 7, 4271–4273.

Graber, H. C., B. K. Haus, R. D. Chapman, and L. K. Shay, 1997: HF radar comparisons with moored estimates of current speed and direction: Expected differences and implications. *Journal of Geophysical Research: Oceans*, **102 (C8)**, 18 749–18 766.

Grosdidier, S., P. Forget, Y. Barbin, and C.-A. Guérin, 2014: HF bistatic ocean Doppler spectra: Simulation versus experimentation. *IEEE Trans. Geosci. and Remote Sens.*, **52 (4)**, 2138–2148.

Guérin, C.-A., D. Dumas, A. Gramoullé, C. Quentin, M. Saillard, and A. Molcard, 2019: The multistatic oceanographic HF radar network in Toulon. *2019 International Radar Conference (RADAR)*, 1–5.

Gurgel, K.-W., G. Antonischki, H.-H. Essen, and T. Schlick, 1999a: Wellen radar (wera): a new ground-wave HF radar for ocean remote sensing. *Coastal engineering*, **37 (3)**, 219–234.

Gurgel, K.-W., Y. Barbin, and T. Schlick, 2007: Radio frequency interference suppression techniques in FMCW modulated HF radars. *OCEANS 2007-Europe*, IEEE, 1–4.

Gurgel, K.-W., H.-H. Essen, and S. Kingsley, 1999b: High-frequency radars: physical limitations and recent developments. *Coastal engineering*, **37 (3)**, 201–218.

Gurgel, K.-W., and T. Schlick, 2005: HF radar wave measurements in the presence of ship echoes-problems and solutions. *Europe Oceans 2005*, IEEE, Vol. 2, 937–941.

Gurgel, K.-W., and T. Schlick, 2009: Remarks on signal processing in HF radars using FMCW modulation. *Proc. IRS*, 1–5.

Gurgel, K.-W., T. Schlick, G. Voulgaris, J. Seemann, and F. Ziemer, 2011: HF radar observations in the german bight: Measurements and quality control. *2011 IEEE/OES 10th Current, Waves and Turbulence Measurements (CWTM)*, IEEE, 51–56.

Headrick, J., and J. Thomason, 1998: Applications of high-frequency radar. *Radio Science*, **33 (4)**, 1045–1054.

765 Kalampokis, A., M. Uttieri, P.-M. Poulain, and E. Zambianchi, 2016: Validation of HF radar-
766 derived currents in the Gulf of Naples with Lagrangian data. *IEEE Geoscience and Remote*
767 *Sensing Letters*, **13 (10)**, 1452–1456, https://doi.org/10.1109/LGRS.2016.2591258.

768 Kirincich, A., 2017: Improved detection of the first-order region for direction-finding hf radars
769 using image processing techniques. *Journal of Atmospheric and Oceanic Technology*, **34 (8)**,
770 1679–1691.

771 Kirincich, A., B. Emery, L. Washburn, and P. Flament, 2019: Improving surface current reso-
772 lution using direction finding algorithms for multiantenna High-Frequency radars. *Journal of*
773 *Atmospheric and Oceanic Technology*, **36 (10)**, 1997–2014.

774 Kohut, J., and S. Glenn, 2003: Improving HF radar surface current measurements with measured
775 antenna beam patterns. *Journal of Atmospheric and Oceanic Technology*, **20 (9)**, 1303 – 1316.

776 Krim, H., and M. Viberg, 1996: Two decades of array signal processing research. *IEEE signal*
777 *processing magazine*.

778 Laws, K., D. Fernandez, and J. Paduan, 2000: Simulation-based evaluations of HF radar ocean
779 current algorithms. *IEEE Journal of Oceanic Engineering*, **25 (4)**, 481–491, https://doi.org/
780 10.1109/48.895355.

781 Lipa, B., and D. Barrick, 1983: Least-squares methods for the extraction of surface currents from
782 codar crossed-loop data: Application at arsloe. *IEEE Journal of Oceanic Engineering*, **8 (4)**,
783 226–253, https://doi.org/10.1109/JOE.1983.1145578.

784 Lipa, B., C. Whelan, B. Rector, and B. Nyden, 2009: Hf radar bistatic measurement of surface
785 current velocities: Drifter comparisons and radar consistency checks. *Remote Sensing*, **1 (4)**,
786 1190–1211.

787 Liu, Y., R. H. Weisberg, and C. R. Merz, 2014: Assessment of CODAR SeaSonde and WERA
788 HF radars in mapping surface currents on the West Florida shelf. *Journal of Atmospheric and*
789 *Oceanic Technology*, **31 (6)**, 1363–1382.

790 Lopez, G., A.-C. Bennis, Y. Barbin, A. Sentchev, L. Benoît, and L. Marié, 2020: Surface currents
791 in the alderney race from high-frequency radar measurements and three-dimensional modelling.
792 *Philosophical Transactions of the Royal Society A*, **378 (2178)**, 20190 494.

Lorente, P., and Coauthors, 2022: Coastal high-frequency radars in the Mediterranean – part 1: Status of operations and a framework for future development. *Ocean Science*, **18 (3)**, 761–795.

Nazari, M. E., W. Huang, and C. Zhao, 2019: Radio frequency interference suppression for HF surface wave radar using cemd and temporal windowing methods. *IEEE Geoscience and Remote Sensing Letters*, **17 (2)**, 212–216.

Novelli, G., C. M. Guigand, C. Cousin, E. H. Ryan, N. J. Laxague, H. Dai, B. K. Haus, and T. M. Özgökmen, 2017: A biodegradable surface drifter for ocean sampling on a massive scale. *Journal of Atmospheric and Oceanic Technology*, **34 (11)**, 2509–2532.

Ohlmann, C., and et. al, 2007: Interpretation of coastal HF radar–derived surface currents with high-resolution drifter data. *Journal of Atmospheric and Oceanic Technology*, **24 (4)**, 666–680.

Paduan, J., and H. Graber, 1997: Introduction to High-Frequency radar: reality and myth. *Oceanography*, **10 (2)**, 36–39.

Paduan, J., and L. Washburn, 2013: High-frequency radar observations of ocean surface currents. *Annual review of marine science*, **5**, 115–136.

Parks, A., L. K. Shay, W. E. Johns, J. Martinez-Pedraja, and K.-W. Gurgel, 2009: HF radar observations of small-scale surface current variability in the straits of florida. *Journal of Geophysical Research: Oceans*, **114 (C8)**.

Querin, S., S. Cosoli, R. Gerin, C. Laurent, V. Malačič, N. Pristov, and P.-M. Poulain, 2021: Multi-platform, high-resolution study of a complex coastal system: The tosca experiment in the gulf of trieste. *Journal of Marine Science and Engineering*, **9 (5)**, 469.

Reyes, E., and Coauthors, 2022: Coastal high-frequency radars in the Mediterranean – part 2: Applications in support of science priorities and societal needs. *Ocean Science*, **18 (3)**, 797–837.

Roarty, H., and Coauthors, 2019: The global high frequency radar network. *Frontiers in Marine Science*, **6**, 164.

Röhrs, J., A. K. Sperrevik, K. Hakon, and v. Broström, Göran andBreivik, 2015: Comparison of HF radar measurements with Eulerian and Lagrangian surface currents. *Ocean Dynamics*, **65**, 679–690.

Rypina, I. I., A. R. Kirincich, R. Limeburner, and I. A. Udovydchenkov, 2014: Eulerian and Lagrangian correspondence of High-Frequency radar and surface drifter data: Effects of radar resolution and flow components. *Journal of Atmospheric and Oceanic Technology*, **31 (4)**, 945 – 966.

Schmidt, R., 1986: Multiple emitter location and signal parameter estimation. *IEEE transactions on antennas and propagation*, **34 (3)**, 276–280.

Sentchev, A., P. Forget, and P. Fraunié, 2017: Surface current dynamics under sea breeze conditions observed by simultaneous HF radar, ADCP and drifter measurements. *Ocean Dynamics*, **67 (3)**, 499–512.

Shay, L. K., J. Martinez-Pedraja, T. M. Cook, B. K. Haus, and R. H. Weisberg, 2007: High-frequency radar mapping of surface currents using WERA. *Journal of Atmospheric and Oceanic Technology*, **24 (3)**, 484–503.

Solomon, I. S., D. A. Gray, Y. I. Abramovich, and S. J. Anderson, 1999: Receiver array calibration using disparate sources. *IEEE Transactions on Antennas and Propagation*, **47 (3)**, 496–505.

Wang, W., and E. W. Gill, 2016: Evaluation of beamforming and direction finding for a phased array HF ocean current radar. *Journal of Atmospheric and Oceanic Technology*, **33 (12)**, 2599 – 2613.

Washburn, L., E. Romero, C. Johnson, B. Emery, and C. Gotschalk, 2017: Measurement of antenna patterns for oceanographic radars using aerial drones. *Journal of Atmospheric and Oceanic Technology*, **34 (5)**, 971–981.

Wei, G., and Coauthors, 2020: Assessment of HF radar in mapping surface currents under different sea states. *Journal of Atmospheric and Oceanic Technology*, **37 (8)**, 1403 – 1422.

Wyatt, L., 2014: High frequency radar applications in coastal monitoring, planning and engineering. *Australian Journal of Civil Engineering*, **12 (1)**, 1–15.

Zhou, H., and B. Wen, 2012: Radio frequency interference suppression in small-aperture high-frequency radars. *IEEE Geoscience and Remote Sensing Letters*, **9 (4)**, 788–792.

Zhou, H., B. Wen, and S. Wu, 2005: Dense radio frequency interference suppression in HF radars. *IEEe signal processing letters*, **12 (5)**, 361–364.